

1  
2  
3  
4  
5  
6  
7  
8  
9  
10  
11  
12  
13  
14  
15  
16  
17  
18

**Variations of Arctic winter ozone from the LIMS Level 3 dataset**

Ellis Remsberg<sup>1</sup>, Murali Natarajan<sup>1</sup>, and Ernest Hilsenrath<sup>2</sup>

<sup>1</sup>Science Directorate, NASA Langley Research Center, 21 Langley Blvd, Mail Stop 401B, Hampton, VA 23681, USA

<sup>2</sup>Fellow at Joint Center for Earth System Technology, University of Maryland at Baltimore County, 1000 Hilltop Circle, Baltimore, MD 21250, USA

Correspondence to: Ellis Remsberg ([ellis.e.remsberg@nasa.gov](mailto:ellis.e.remsberg@nasa.gov))

(for submission to Atmospheric Measurement Techniques Journal)

February, 2022

19

20 **Abstract**

21 The Nimbus 7 limb infrared monitor of the stratosphere (LIMS) instrument operated from  
22 October 25, 1978, through May 28, 1979. Its Version 6 (V6) profiles and their Level 3 or zonal  
23 Fourier coefficient products have been characterized and archived in 2008 and in 2011,  
24 respectively. This paper focuses on the value and use of daily ozone maps from Level 3, based  
25 on a gridding of its zonal coefficients. We present maps of V6 ozone on pressure surfaces and  
26 compare them with several rocket-borne chemiluminescent ozone measurements that extend into  
27 the lower mesosphere. We illustrate how the synoptic maps of V6 ozone and temperature are an  
28 important aid in interpreting satellite limb-infrared emission versus local measurements,  
29 especially when they occur during dynamically active periods of northern hemisphere winter. A  
30 map sequence spanning the minor stratospheric warmings of late January and early February  
31 characterizes the evolution of a low ozone pocket (LOP) at that time. We also present time  
32 series of the wintertime tertiary ozone maximum and its associated zonally varying temperatures  
33 in the upper mesosphere. These examples provide guidance to researchers for further  
34 exploratory analyses of the daily maps of middle atmosphere ozone from LIMS.

35

36 **1 Introduction and objectives**

37 The historic Nimbus 7 Limb Infrared Monitor of the Stratosphere (LIMS) experiment provided  
38 data on middle atmosphere ozone from October 25, 1978, through May 28, 1979, for scientific  
39 analysis and for comparisons with atmospheric models (Gille and Russell, 1984). Ozone is an  
40 excellent tracer of stratospheric transport in the high latitude stratosphere. As an early example,  
41 Leovy et al. (1985) showed how daily maps of the LIMS ozone fields correlate well with  
42 geopotential height (GPH) fields on the 10-hPa pressure surface. They also reported on the  
43 rapidly changing effects of wave activity on ozone, which led to a better understanding of  
44 stratospheric transport processes within models. Hitchman et al. (1989) also analyzed the  
45 temperature fields from LIMS and reported on Arctic observations of an elevated stratopause in  
46 late autumn to early winter that they associated with momentum forcings from gravity waves.

47

48 Current research focuses on the 3-dimensional character of ozone in the upper stratosphere and  
49 mesosphere, based on more recent satellite datasets. Several studies consider how temperature  
50 and ozone vary in association with sudden stratospheric warming (SSW) events (Smith et al.,  
51 2009; de la Camara et al., 2018; Kim et al., 2020; Shams et al., 2021). Manney et al. (1995) and  
52 Harvey et al. (2008) describe the development of low ozone pockets (LOPs) in the region of the  
53 Aleutian anticyclone during winter. Siskind et al. (2005; 2021) explain the occurrence of a  
54 mesospheric cooling associated with SSWs and the role of gravity waves for modeling ozone in  
55 the upper mesosphere, respectively. Chandran et al. (2013) provide a climatology of the Arctic  
56 elevated stratopause, and Sofieva et al. (2021) analyze for regional trends in stratospheric ozone.  
57 Smith et al. (2011; 2018) report on monthly changes of the tertiary ozone maximum at high  
58 latitudes of the upper mesosphere during winter.

59

60 The LIMS (Level 2) profiles were retrieved with an improved Version 6 (V6) algorithm. They  
61 were archived in 2008 and include ozone, temperature, and GPH that extend from 316 hPa to  
62 ~0.01 hPa. Co-located V6 profiles of water vapor ( $\text{H}_2\text{O}$ ), nitric acid vapor ( $\text{HNO}_3$ ), and nitrogen  
63 dioxide ( $\text{NO}_2$ ) extend through the stratosphere. Lieberman et al. (2004) analyzed the V6  
64 temperature profiles and found evidence for non-migrating tides in the mesosphere, due to the  
65 interaction of the diurnal tide and planetary zonal-wave 1, especially in late January 1979. Holt  
66 et al. (2010) analyzed the descent of V6  $\text{NO}_2$  from the lower mesosphere to within the polar  
67 stratospheric vortex, where it interacts with ozone. Remsberg et al. (2013) assimilated V6 ozone  
68 profiles in a reanalysis model and gained improved estimates of column ozone, especially in  
69 Arctic winter. Such reanalysis studies assimilate temperature and ozone profiles within a model  
70 framework. However, the models only approximate the effects of small-scale variations, so it is  
71 also useful to consider observed variations of the LIMS parameters without resort to a model.  
72 Keep in mind that smaller-scale atmospheric variations also contribute to the analyzed  
73 intermediate and large-scale fields from V6. This paper further explores several instances of  
74 those larger-scale variations of Arctic ozone, temperature, and GPH.

75

76 The SPARC Data Initiative (SPARC-DI) includes monthly zonal averages of V6 ozone up to the  
77 0.1-hPa level (see Tegtmeier et al., 2013; SPARC, 2017; and Remsberg et al., 2021). In Section

78 2 we show January zonal averages of V6 ozone and temperature profiles that extend even higher  
79 or to near the mesopause. The V6 Level 3 (map) product provides a 3-dimensional context for  
80 those zonal mean data. Daily V6 maps are also an aid in interpreting individual V6 profiles  
81 versus correlative data, especially during dynamically disturbed periods. Specifically, in Section  
82 3 we compare several nighttime V6 ozone profiles with those obtained with a rocket-borne  
83 chemiluminescent technique (Hilsenrath et al., 1980). Those profile comparisons are for  
84 December 15 and for January 27 and 28, when the temperature and ozone fields were affected by  
85 planetary wave forcings. There is a corresponding cooling and variations of ozone in the winter  
86 lower mesosphere associated with the warming in the upper stratosphere. Section 4 presents  
87 variations of ozone and GPH at northern extratropical latitudes during the minor SSW events of  
88 late January and early February 1979, as a complement to the more comprehensive findings of  
89 Harvey et al. (2008) on the occurrence of LOPs within anticyclones determined from satellite  
90 solar occultation data. Section 5 considers the variability of the tertiary ozone maximum in the  
91 upper mesosphere during that same period, as an adjunct to monthly zonal average values  
92 reported by Smith et al. (2018). Section 6 notes that the maps of V6 ozone contain more details  
93 about gradients in temperature and ozone and cautions users about occasional, pseudo-ozone  
94 features in the tropical lowermost stratosphere. Section 7 concludes that the V6 Level 3 product  
95 is an important resource for studies of the effects of transport and chemistry on Arctic ozone.

96

## 97 **2 Characteristics of V6 Level 3 data**

### 98 *2.1 LIMS measurements and analyses*

99 Nimbus 7 was in a near-polar orbit, and LIMS made measurements at ~1 pm local time along its  
100 ascending (A or south-to-north) orbital segments and at ~11 pm on its descending (D or north-to-  
101 south) segments. A-D time differences are of the order of 10 hours at most latitudes because  
102 LIMS viewed the atmosphere 146.5° clockwise of the spacecraft velocity vector, as seen from  
103 above. The A-D differences narrow from 10 to about 6 hours from 60°N to 80°N, due to the  
104 orbital geometry of Nimbus 7. The V6 processing algorithm accounts for low-frequency  
105 spacecraft motions that affect the LIMS view of the horizon. As a result, its measured radiance  
106 profiles are well registered in pressure-altitude (Remsberg et al., 2004). Retrieved V6 ozone,  
107 temperature, and GPH profiles extend from 316 hPa to ~0.01 hPa and have a vertical point

108 spacing of  $\sim 0.88$  km with an altitude resolution of  $\sim 3.7$  km. Retrieved profile pairs are spaced  
109 every 144 km along the orbital track or at every  $1.3^\circ$ , but closer together at the high, turn-around  
110 latitudes of the orbital viewing geometry (Remsberg et al., 1990). LIMS made measurements  
111 with a duty cycle of about 11 days on and 1 day off over its planned observing lifetime. The  
112 LIMS algorithms (Remsberg et al., 2007) do not account for non-local thermodynamic  
113 equilibrium (NLTE) effects in ozone (Solomon et al., 1986; Mlynczak and Drayson, 1990) and  
114 in  $\text{CO}_2$  (Edwards et al., 1996; Manuilova et al., 1998), so there are positive biases in the retrieved  
115 V6 ozone throughout the mesosphere during daylight. However, the V6 nighttime ozone is more  
116 nearly free of NLTE effects below about the 0.05-hPa level, except at times of SSWs (see e.g.,  
117 Funke et al., 2012).

118  
119 A sequential-estimation (SE) algorithm was used to generate daily, zonal Fourier coefficients  
120 (zonal mean and up to six cosine and sine values or 6-zonal wavenumbers) for Level 3 at every  
121  $2^\circ$  of latitude and at up to 28 vertical levels (Remsberg and Lingenfelser, 2010). The V6 SE  
122 algorithm uses better estimates of data uncertainty and its zonal wave coefficients have a  
123 memory of  $\sim 2.5$  days, or about half that of the SE algorithm used by Remsberg et al. (1990).  
124 The SE analysis is insensitive to the very few large, unscreened ozone profile values found in  
125 the lower stratosphere, as noted in Remsberg et al. (2013, their Fig. 1a). The SE algorithm  
126 combines the coefficients from both the separate A and D orbital segments and effectively  
127 interpolates the profile data in time to provide a continuous, 216-day set of daily zonal  
128 coefficients versus pressure-altitude at 1200Z for each of the retrieved LIMS parameters.

129

## 130 *2.2 Monthly average V6 data*

131 One can generate monthly average distributions from the daily Level 3 files of temperature,  
132 GPH, and species (ozone,  $\text{H}_2\text{O}$ ,  $\text{HNO}_3$ , and  $\text{NO}_2$ ); zonal averages for the V6 species were  
133 supplied to SPARC-DI (SPARC, 2017; Hegglin et al., 2021). Tegtmeier et al. (2013) compared  
134 the V6 monthly ozone distributions with ones from other satellite-based, limb sensors and  
135 reported good agreement throughout the stratosphere. Although the species cross sections for  
136 SPARC (2017) extend only up to the 0.1-hPa level ( $\sim 64$  km), V6 average ozone extends higher

137 or to about 0.015 hPa ( $\sim 75$  km). Figure 1 shows the latitude-pressure cross section for January  
138 from just the descending (D) orbital profiles, which avoids the larger NLTE biases that affect  
139 daytime ozone in the mesosphere. Stratospheric ozone mixing ratios in Fig. 1 have largest  
140 values at about 10 hPa near the Equator ( $> 9.2$  ppmv), and they decrease sharply above and  
141 below that level. Maximum mixing ratios for the middle to high latitudes occur between 3 to 5  
142 hPa, due to the larger zenith angles and longer paths of the ultraviolet light for production of  
143 atmospheric ozone. There is a nighttime ozone minimum of  $\sim 1.2$  ppmv across most latitudes of  
144 the middle mesosphere. A tertiary ozone maximum is present in the upper mesosphere near the  
145 winter day/night terminator zone in the LIMS measurements for January (at about  $67^\circ\text{N}$ ), in  
146 accordance with the interpretation of Marsh et al. (2001). The location ( $\sim 0.02$  hPa) and  
147 magnitude ( $\sim 3.5$  ppmv) of the NH maximum are somewhat higher and larger than those reported  
148 by Smith et al. (2018, their Fig. 4) from more recent satellite datasets. Although the V6 ozone  
149 poleward of  $\sim 55^\circ\text{S}$  is also from descending orbital profiles, it corresponds to daylight conditions  
150 at the high southern latitudes in January. Thus, the decrease of mesospheric V6 ozone at 0.1 hPa  
151 and poleward of  $55^\circ\text{S}$  indicates merely a change from night to day values and agrees with  
152 findings of Lopez-Puertas et al. (2018). On the other hand, the rather large ozone values in the  
153 upper mesosphere at about  $45^\circ\text{S}$  are not found in other data sets and are not expected from  
154 theory. We consider that ozone anomaly further in Section 6.

155

156 Radiances from two  $15\text{-}\mu\text{m}$   $\text{CO}_2$  channels are used for retrievals of V6 temperature versus  
157 pressure or  $T(p)$ , and they are free of NLTE effects below about the 0.05-hPa level ( $\sim 70$  km)  
158 (Lopez-Puertas and Taylor, 2001). To first order, the V6  $T(p)$  retrievals account for the effects  
159 of horizontal temperature gradients in the stratosphere (Remsberg et al., 2004). Single profile  
160 root-sum-squared (or RSS) errors for  $T(p)$  vary from 1 K at 10 hPa to  $\sim 2.5$  K in the upper  
161 mesosphere, but they do not include possible temperature gradient errors. RSS error from  $T(p)$  is  
162 the primary source of bias error for ozone, growing to about 16% in the middle mesosphere  
163 (Remsberg et al., 2021, Table 1). Random errors become large for single ozone profiles in the  
164 upper mesosphere. As a complement to the V6 ozone of Fig. 1, we show the descending  
165 ( $\sim$ nighttime) V6  $T(p)$  distribution for January in Figure 2, which extends to near the 0.01-hPa  
166 level. The large-scale features of the  $T(p)$  distribution compare well with climatological values

167 from the late 1970s (Fleming et al., 1990), having a maximum value of about 285 K at the SH  
168 high latitude stratopause and minimum values of  $< 200$  K at the tropical tropopause and near the  
169 SH summer mesopause. There is also some elevation of the Arctic zonal-average stratopause.

170

171 Figure 3 shows the monthly-average, zonal (wave) standard deviations (SD) about daily zonal  
172 means of the combined-mode (A+D) V6 ozone for January, where the SD values are derived  
173 from the zonal-wave amplitudes of V6 Level 3. There are relatively small SD values at low  
174 latitudes from 7 to 10 hPa; it is assumed that they are a result of smaller-amplitude Kelvin and  
175 Rossby-gravity waves. Effects of more vigorous, planetary wave activity are most apparent at  
176 high northern latitudes of the stratosphere during winter. Gravity waves also contribute to SD in  
177 the uppermost mesosphere (Siskind et al., 2021). Ozone shows little zonal variation in the SH  
178 upper stratosphere of Fig. 3, due to constraints on the upward propagation of planetary waves  
179 through the summer zonal easterlies (Andrews et al., 1987). SD values near the tropical  
180 tropopause are due mostly to residual effects of emissions from thin cirrus and represent spurious  
181 ozone variations (see Section 6).

182

### 183 **3. V6 comparisons with rocket-borne chemiluminescent ozone measurements**

184 In this section we consider V6 comparisons with three nighttime, rocket-borne chemiluminescent  
185 ozone soundings of Hilsenrath (1980)—one at White Sands, NM, (32.4°N, 253.5°E) on  
186 December 15, 1978, and two more at Poker Flat, AK, (65.1°N, 212.5°E) on the successive days  
187 of January 27 and 28, 1979. The estimated total, rocket ozone error is 14% (precision plus  
188 accuracy), according to Hilsenrath and Kirschner (1980).

189

190 Ozone comparisons for December 15 are in Figure 4 (top); we plot every other V6 profile and  
191 those four profiles have spacings of 2.6° in latitude. The short-dashed V6 profile is at 29.2°, and  
192 the long-dashed profile is at 37.2°. The solid curve is the V6 profile at 31.8° (at 0611Z) or  
193 closest to the rocket sounding from White Sands (at 0541Z). Horizontal bars on the profiles are  
194 estimates of ozone error; they overlap between V6 and rocket, except in the upper stratosphere.

195 LIMS ozone is larger than rocket ozone in through the upper stratosphere. The corresponding  
196 V6 ozone map at 4.6 hPa in Fig. 4 (bottom) reveals an ozone maximum just south of White  
197 Sands (WS—blue dot), along the descending orbital segment of the satellite at (6°N, 265°E—  
198 white dot) or viewing in the NNW direction toward White Sands. Note that while zonal  
199 variations in the map are from a gridding of the Level 3 coefficients (2° latitude and 5.625°  
200 longitude), there is no smoothing of the gridded field in the meridional direction; there is good  
201 continuity across latitudes, nonetheless. The rocket profile is a local measurement and has a  
202 vertical resolution that ranges from 1.5 km at 60 km to 0.1 km at 20 km; the nearby V6 profiles  
203 have a lower vertical resolution of ~3.7 km and are an average over the finite horizontal length  
204 (~300 km or ~3° latitude) of the LIMS tangent layer. There is an ozone maximum along the  
205 LIMS view path just to the south of White Sands, which may account for the profile differences.  
206 We also note that the ozone field of two days earlier has the region of sharp gradients positioned  
207 over White Sands with ozone at only 8 ppmv. Thus, an ozone field that varies in both space and  
208 time can lead to additional uncertainties for comparisons of the localized rocket and limb-  
209 viewing satellite profiles in Fig. 4.

210

211 Because V6 ozone is obtained from retrievals of the measured V6 ozone radiance profiles, the  
212 LIMS retrieved temperature profile must be representative of the atmospheric state for the  
213 forward model of ozone radiance. Figure 5 (top) shows the corresponding temperature  
214 comparisons between V6 and a separate rocket Datasonde instrument. Agreement between them  
215 is very good throughout the upper stratosphere, indicating that the temperature variations are  
216 well determined along the LIMS view path for the forward radiance calculations of V6 ozone  
217 and that the retrieved V6 ozone should be nearly unaffected by temperature bias error. The map  
218 of V6 temperature (Fig. 5—bottom) shows zonal variations on December 15, although their  
219 meridional gradients are relatively weak above White Sands. Conversely, the ozone profiles  
220 agree well near 0.68 hPa in Fig. 4, where there are apparent biases between the T(p) profiles.  
221 There are significant horizontal gradients near White Sands in the maps of T(p) at 0.68 hPa, but  
222 not in ozone (not shown). In fact, the V6 ozone field at that level has a nearly constant value,  
223 and ozone is less sensitive (by half) to changes in T(p) at 0.68 hPa than at 4.6 hPa (Remsberg et



224 al., 2007). Co-location is more important for the V6 versus rocket comparisons of T(p) than of  
225 ozone in the lower mesosphere.

226

227 The two comparisons above Poker Flat, AK, occurred at the time of a stratospheric, zonal wave-  
228 1 warming event. Leovy et al. (1985) provide a detailed discussion of the advective changes for  
229 ozone in the middle stratosphere during January 1979. Figure 6 (top) shows three V6 ozone  
230 profiles from along an ascending orbital segment on January 27. The LIMS instrument was  
231 viewing from its satellite location (80.7°N, 113°E) at 2204Z, and the rocket ozone launch was  
232 two hours earlier or at 2005Z at a solar zenith angle of 84° or near the terminator; there is good  
233 agreement of the structure between them, even in the mesosphere. A second rocket launch  
234 followed at 0833Z of January 28 (Hilsenrath, 1980). Since the separate V6/rocket ozone and  
235 T(p) comparisons are similar for the two days, Fig. 6 contains results for January 27 only. The  
236 rocket sounding recorded two ozone maxima, one near 15 hPa and another at about 0.6 hPa. The  
237 ozone maximum at about 15 hPa is primarily due to advection of ozone of higher mixing ratios  
238 from lower latitudes just prior to the warming event. The local maximum at 0.6 hPa was  
239 unexpected, based on findings from a larger set of rocket ozone soundings. There is a relative  
240 minimum for both V6 and rocket ozone through the upper stratosphere, although V6 ozone is  
241 larger. The map of V6 ozone at 4.6 hPa in Fig. 6 (bottom) indicates that the rocket measurement  
242 occurs at the center of the minimum, whereas the V6 profiles are averages across it. The ozone  
243 profiles in Fig. 6 (top) indicate the relative minimum in a low-ozone pocket (LOP) that extends  
244 from about 7 hPa to 2 hPa.

245

246 Figure 7 (top) shows the V6 temperature profile comparisons; T(p) from the Datasonde has more  
247 vertical structure, as expected from a localized measurement. V6 T(p) values reach a maximum  
248 of order 250 K at about 3 to 4 hPa. They agree reasonably with the Datasonde values, given that  
249 there is significant horizontal structure in the temperature field surrounding Poker Flat. The  
250 apparent V6 minus Datasonde bias of order 5 K at 3 hPa ought to lead to a V6 minus rocket  
251 ozone bias of -40%, according to error estimates for retrieved V6 ozone. However, Fig. 7  
252 (bottom left) indicates that LIMS was viewing Poker Flat across an area of higher temperatures,  
253 such that it is likely that there is a spatial mismatch for V6 and Datasonde T(p) values. The

254 much smaller and positive ozone differences in Fig. 6 support that likelihood. There may also be  
255 co-location differences between the rocket temperature and ozone soundings in this instance.

256

257 Figure 7 also shows a map of NH GPH at 4.6 hPa on January 27 for comparison with the ozone  
258 map in Fig. 6. Lowest ozone values are in the polar vortex, where the GPH field is asymmetric  
259 about the Pole. A second, low value of ozone is associated with the anticyclone over the  
260 Alaskan sector. One can determine horizontal winds from gradients of GPH on the 4.6-hPa  
261 surface and thereby estimate the transport of ozone to first order. Qualitatively, the direction and  
262 strength of the large-scale transport follows from the character of the cyclonic and anticyclonic  
263 features on the GPH map. The large-scale cyclonic circulation about the vortex transports air  
264 from middle latitudes to across the Pole on January 27. The vortex region has low ozone and is  
265 relatively cold, whereas stratospheric temperatures over Alaska show a maximum (the SSW),  
266 and the rocket profile above Poker Flat, AK, was near the center of the anticyclone and in the  
267 region of relatively low ozone (or LOP).

268

269 Ozone is an approximate tracer of transport processes and reveals dramatic changes with altitude  
270 associated with this SSW event, even through the winter lower mesosphere. As an example,  
271 Figure S1 (in Supplemental Materials) shows a concurrent cooling at 0.46 hPa above the Alaskan  
272 anticyclone on January 27, where the co-located ozone field exhibits a local maximum. There is  
273 also a major temperature increase above the polar stratospheric vortex over northern Europe at  
274 0.46 hPa, or where ozone values remain low. In summary, Figs. 4 through 7 and S1 indicate the  
275 utility of daily maps from LIMS for analyses of the ozone fields during dynamically disturbed  
276 conditions.

277

#### 278 **4. Variation of a low ozone pocket (LOP) from LIMS Level 3**

279 The polar vortex on January 27 was located over northern Europe and Asia; it was centered off  
280 the Pole because of effects of large-scale, planetary waves in the development of the SSW  
281 (Andrews et al., 1987, Chapter 6). In this section, we show sequences of polar plots of both

282 stratospheric GPH and ozone for February 1979. Manney et al. (1995) and Harvey et al. (2004,  
283 2008) provide comprehensive analyses about the occurrence of polar anticyclones and their  
284 associated LOPs from studies of GPH and ozone fields from several different satellites. They  
285 determined the extent and character of the polar vortex based on meteorological data from the  
286 UK Met Office or as obtained from relatively low vertical resolution radiance profiles from  
287 operational, nadir temperature sounders. The V6 GPH profiles are derived from and have the  
288 same vertical resolution as the T(p) profiles. Manney et al. (1995) showed that water vapor is a  
289 useful tracer of the meridional transport of air, and the V6 H<sub>2</sub>O fields at 6.8 and 10 hPa indicate  
290 that low latitude air was transported to the region of the LOP in late January. But the V6 H<sub>2</sub>O  
291 fields are noisy at 4.6 hPa (not shown). Even so, the V6 Level 3 ozone, T(p), and GPH data  
292 offer useful details about the occurrence of LOPs in the upper stratosphere.

293

294 Harvey et al. (2004) reported that LOPs occur nominally at about the 5-hPa level. Accordingly,  
295 the three panels of Figure 8 show three daily NH maps of V6 GPH from February 3 to February  
296 17 at 4.6 hPa; each successive map is spaced one week from the previous one. This sequence  
297 shows that both the vortex and anticyclone weaken during the three weeks following January 27  
298 at this level. The vortex re-centers on the Pole by February 17, and the anticyclone is nearly  
299 absent at 4.6 hPa following the two minor warming events. The map sequence of GPH indicates  
300 that there were significant changes in the horizontal transport of ozone in late January/early  
301 February. The corresponding three panels of ozone in Figure 9 show the further evolution of  
302 ozone, following that of January 27 (in Fig. 6). Even though the anticyclone had weakened  
303 during the first week, there was a deepening of the LOP from January 27 to February 3 and a  
304 filling of it thereafter.

305

306 Was there some chemical loss of ozone from January 27 to February 3 in the region of the LOP?  
307 Morris et al. (1998) and Nair et al. (1998) conducted model calculations to show how that could  
308 happen. Ozone reactions are affected by changes with latitude of solar insolation, temperature,  
309 and loss via NO<sub>x</sub>. Nair et al. (1998) reported on the effect of a decrease in the production of  
310 ozone for the development of LOPs, as air parcels in the middle stratosphere move from low to  
311 high latitudes or to higher solar zenith angles in winter. Remsberg et al. (2018) analyzed air

312 parcel trajectories that included chemistry, and they showed that there was some loss of ozone in  
313 the middle stratosphere, due to reactions with  $\text{NO}_x$ . However, Holt et al. (2012) analyzed V6  
314  $\text{NO}_2$  in the winter polar vortex, and they did not find enhanced values at 4.6 hPa due to energetic  
315 particle precipitation (EPP) by late January.

316

317 Figure 10 (left) is a map of the V6 descending orbital (nighttime)  $\text{NO}_2$  for January 27 at 4.6 hPa.  
318 Based on the corresponding map of GPH in Fig. 7, one can trace the horizontal advection of high  
319  $\text{NO}_2$  toward higher latitudes and toward the polar vortex as well as the advection of low  $\text{NO}_2$  out  
320 of the vortex and about the anticyclone. Fig. 10 (right) is a map of  $\text{HNO}_3$  at 4.6 hPa, and it  
321 shows a weak, relative maximum above the anticyclone.

322

323 The formation of the LOP at 5hPa near Poker Flat region in January is studied with the help of  
324 photochemical calculations along a trajectory. A full description of the trajectory and  
325 photochemical models is given in Remsberg et al (2018). For this study, we generated backward  
326 trajectory starting at 5 hPa and  $212^\circ$  E and  $64^\circ$ N. The starting time of the back trajectory is 0900  
327 Z on January 28,1979. This is close to local time of LIMS descending mode observation of  
328 around 11:00 pm on January 27. Figure 11 shows the back trajectory with the day numbers  
329 illustrating the progress of the air parcel. Between January 22 and 28, the air parcel remains  
330 confined within a small region at high latitude. Results of a time dependent photochemical  
331 calculation conducted along this trajectory in the forward direction are shown in Figure 12 as a  
332 function of time. The model initialization uses the mixing ratios of  $\text{O}_3$ ,  $\text{NO}_2$ , and  $\text{HNO}_3$  from  
333 LIMS descending mode observations. Figure 12 shows that the parcel was at 3 hPa on January  
334 15 and descended steadily to 5 hPa by late January. The decrease in ozone during the last 8 days  
335 is mainly caused by the daytime odd oxygen loss due to the catalytic cycle involving  $\text{NO}_x$ .  
336 Production of odd oxygen is minimized since the air parcel is confined to high latitudes. Large  
337 diurnal variations in  $\text{NO}_2$  and a small increase in  $\text{HNO}_3$  are as expected for this pressure level.  
338 The LOP formation is a result of the interplay between transport and photochemistry in the high  
339 latitude upper stratosphere in the winter.

340

## 341       **5. Variations of the tertiary ozone maximum**

342 Smith et al. (2018) describe the changing monthly, zonally averaged character of the wintertime  
343 tertiary ozone maximum of the polar upper mesosphere. They point out that the low latitude  
344 edge of the tertiary ozone maximum is where HO<sub>x</sub> radicals and the chemical loss of ozone due to  
345 reactions with them are reduced. V6 ozone radiance profiles have low signal-to-noise in the  
346 upper mesosphere; the precision estimate is 0.32 ppmv for retrieved ozone profiles. We show a  
347 map in Figure 13 of the combined V6 ozone for December 15 at 0.022 hPa (~72 km), where its  
348 distribution in the subpolar region is based on fewer than 13 zonal coefficients because some  
349 profiles do not extend to that pressure altitude. The corresponding map of temperature is also in  
350 Fig. 13, and one can see that there is significant non-zonal structure in its field at the latitudes  
351 where ozone is enhanced. While both V6 ozone and temperature are not highly accurate due to  
352 NLTE effects in the upper mesosphere, their maps reveal significant relative spatial structures  
353 indicating advective transport and its likely effects on ozone.

354

355 Figures S2 and S3 in the Supplemental Materials show additional panels at 0.022 hPa of ozone  
356 and temperature, respectively, for January 13, February 10, and March 1. Elevated values of  
357 ozone occur at higher latitudes on February 10 and March 1 than on December 15 and January  
358 13, which is consistent with the more northward position of the terminator away from winter  
359 solstice and the consequent effects for the chemical loss of ozone. The temperature fields are  
360 also perturbed on January 13 and February 10, but they are more nearly zonal by March 1.  
361 However, there are meridional gradients of temperature on all three days in the region of the  
362 tertiary ozone maximum. On January 13 there is also a well-defined mesospheric vortex in GPH  
363 (not shown), and the highest values of ozone correlate reasonably with it. The vortex is most  
364 disturbed and tertiary ozone maximum has largest values on February 10, perhaps in response to  
365 the upward propagation of wave activity following the minor SSW of late January.

366

367 Figure 14 shows time series of peak zonal mean ozone at 0.022 hPa and its latitude location for  
368 each week from November through mid-March. The separate time series are for peak ozone  
369 (bottom two series) and their latitude locations (top two). Dashed red curves represent zonal

370 mean results for combined (A+D) ozone; solid black curves are results for nighttime (D) only.  
371 Blue horizontal lines represent the approximate latitude position of the terminator. Peak  
372 nighttime ozone values are based on just the ‘zonal mean’ and the cosine and sine coefficients  
373 for waves 1 and 2 because not all profiles reach to the 0.022-hPa level. Peak ozone occurs at  
374 lower latitudes ( $\sim 65^\circ\text{N}$ ) in December, increasing to  $\sim 75^\circ\text{N}$  in early November and early February  
375 and to near  $80^\circ\text{N}$  by early March. The latitude time series of peak ozone values is reasonably  
376 coincident with the changing location of the terminator. Peak combined (A+D) ozone increases  
377 slowly from a minimum of 2.2 ppmv in November to 3.6 ppmv in late February and March.  
378 Descending (or nighttime only) ozone varies from 3.3 ppmv in November, to  $\sim 4.5$  ppmv in  
379 January, to a maximum of 6.3 ppmv in mid-February, and then declining to 3.5 ppmv by mid-  
380 March, although the time series shows rather large variations. Those maximum V6 values are  
381 larger than reported by Lopez-Puertas et al. (2018, their Fig. 15), perhaps due to biases from V6  
382 T(p) and/or ozone at 0.022 hPa.

383  
384 The increase of V6 ozone during winter in Fig. 14 disagrees with that of Smith et al. (2018), who  
385 found decreasing ozone by February. They reported that, in most years, there is a slow descent  
386 of relatively dry air into the vortex region in the upper mesosphere during late autumn and early  
387 winter, and that the reduction in water vapor implies that there are fewer  $\text{HO}_x$  radicals for the  
388 destruction of ozone near the terminator zone, leading to accumulations of ozone. However,  
389 there were two minor warmings and associated lower mesospheric cooling events during late  
390 January and early February 1979 (Hitchman et al., 1989). The enhanced V6 ozone of February  
391 1979 follows those SSW events, and there are wave-driven disturbances and dissipation of their  
392 energy in the upper mesosphere at that time (e.g., Siskind et al. 2005; Smith et al., 2009). One  
393 can gain more details about the evolution of the tertiary ozone maximum in the winter of 1978-  
394 79 from the daily maps of V6 ozone, T(p), and GPH (as in Figs. S2 and S3).

395

## 396 **6. Other aspects of V6 Level 3 ozone**

397 The combined (A+D) Level 3 coefficients are the basis for a gridding of daily synoptic maps at  
398 1200Z of ozone and related parameters. The Level 3 product also contains coefficients from its

399 separate A and D profiles; their ‘zonal mean’ values correspond to the local time-of-day of their  
400 respective measurements. Remsberg et al. (2007) noted that maps from V6 reveal more details  
401 about the variations of ozone. In Figure S4 of the Supplemental Materials we compare a map of  
402 V6 ozone at 10 hPa on 27 January with a similar map for V5 of Leovy et al. (1985). The ozone  
403 gradients are more pronounced with V6 than with V5 at both the subtropical and vortex edges of  
404 the ozone field. The V6 maps make use of all profiles along the orbit, and the SE mapping  
405 algorithm was applied to them every 2° of latitude. However, the tighter gradients were also  
406 achieved with the V6 algorithm because it has a relaxation time (or memory) that is half that of  
407 V5. This means that the V6 maps are more representative of the rapidly changing atmospheric  
408 ozone fields on that day. Similar version differences are evident throughout winter, when the so-  
409 called ‘stratospheric surf zone’ develops and expands (Leovy et al., 1985).

410

411 Significant exchanges of air and ozone occur from the extratropical stratosphere to the  
412 troposphere in winter and spring (Gettelman et al., 2011). There are large zonal variations about  
413 the daily zonal means of ozone in the Arctic region of the lower stratosphere in Fig. 3. There are  
414 similar variations in GPH (and derived winds) and in zonal wave activity that lead to ozone  
415 transport. Zonal variations are resolved in the daily ozone maps down to the 146-hPa level.  
416 Notably, Shepherd et al. (2014) integrated the V6 monthly zonal mean ozone above the  
417 tropopause and subtracted it from observed total ozone, as part of their assessment of long-term  
418 trends of tropospheric ozone from models. Their determination of extratropical tropospheric  
419 ozone based on LIMS agrees with that obtained from other ozone datasets.

420

421 There is also a relative excess of SD ozone values in Fig. 3 centered at 68 hPa at tropical  
422 latitudes, and similar anomalies occur in other LIMS months (not shown). As an example,  
423 Figure 15 shows a map of V6 ozone at 68 hPa (~18 km) on December 15, to give more insight  
424 about the source of the tropical variations. Ozone mixing ratio values in Fig. 15 are of order 2 to  
425 3 ppmv at high latitudes, becoming much smaller in the subtropics. However, there is also an  
426 unexpected, high value of 2 to 3 ppmv at about 15°N, 150°E. Limb measurements in the ozone  
427 channel include radiance effects from cirrus particles that can occur along the tangent view path,  
428 although the retrieved ozone mixing ratio profiles were screened of those effects to first order

429 (Remsberg et al., 2007). Even so, we note that ozone is easily affected by any excess radiance  
430 because of highly non-linear effects for retrievals of ozone in the lower stratosphere. It is very  
431 likely that the anomalous ozone at 68 hPa is a result of residual effects from subvisible cirrus,  
432 which is nearly ubiquitous over the western tropical Pacific region (see SPARC, 2006, Fig. 1.8).  
433 While individual V6 ozone profiles may include such spurious features in the tropics, the Level 3  
434 ozone product at 68 hPa is affected mainly when there is an organized convection and outflow of  
435 air that persists for several days. The adjacent map of ozone at 46 hPa appears unperturbed in  
436 that region (not shown), and tropical ozone at 100 hPa approaches zero. There are much smaller  
437 anomalies in maps of nitric acid, as its mixing ratio retrieval is very nearly linear. Anomalies are  
438 also not so apparent in maps of V6 H<sub>2</sub>O at 68 hPa because the cloud screening algorithm for H<sub>2</sub>O  
439 accounts for the larger vertical field-of-view and extent in altitude for measurements in the water  
440 vapor channel of LIMS. Thus, one must be mindful that the Level 3 product may indicate  
441 excess, but spurious ozone at 68 hPa in the tropics.

442

443 Finally, in our earlier description of descending orbital ozone in Fig. 1, we noted that there are  
444 anomalously high values near 45°S in the upper mesosphere. Fig. S5 of the Supplemental  
445 Materials shows distributions of temperature and ozone from descending orbital measurements at  
446 0.032 hPa on January 15. Zonal wave activity is very weak in both. The descending orbital  
447 views of the tangent layer at 45°S are located just in front of the region of large temperature  
448 gradients at 40°S. Although we showed in Section 3 that taking account of temperature  
449 gradients is important for accurate retrievals of ozone, such gradients were not employed for  
450 calculations in the mesosphere of tangent layer radiance in the V6 algorithms. If such  
451 temperature biases persist through the upper mesosphere, they will also affect the registration of  
452 the observed ozone radiance versus pressure at those altitudes. Therefore, we judge that it is  
453 very likely that the enhanced ozone mixing ratios near 45°S in Fig. 1 are an artifact because the  
454 associated, retrieved tangent path temperatures are not weighted properly, are too cold, and do  
455 not account for enough of the observed ozone radiance. Ozone mixing ratio anomalies are not  
456 apparent along the ascending orbital segment because their LIMS views are in a near-zonal  
457 direction.

458



## 459 7. Conclusions

460 This report provides guidance to researchers for their use of the LIMS V6 Level 3 product and  
461 for their generation of daily gridded distributions of its temperature, ozone, and GPH on pressure  
462 surfaces. H<sub>2</sub>O, NO<sub>2</sub>, and HNO<sub>3</sub> are also available for the stratosphere from the Level 3 product.  
463 The V6 dataset represents an early baseline for considering possible changes in the middle  
464 atmosphere from 1979 to today and into the future. LIMS made measurements at a time when  
465 stratospheric effects from volcanoes were minimal and when catalytic effects of chlorine on  
466 ozone were relatively small. Accordingly, Stolarski et al. (2012) found small, but significant  
467 changes in the distribution of upper stratospheric ozone for recent decades compared with 1978-  
468 1979. The LIMS measurements were taken near solar maximum and when atmospheric  
469 concentrations of the greenhouse gases (GHG), CO<sub>2</sub>, CH<sub>4</sub>, and CFCs, were smaller than today.  
470 Middle atmosphere T(p) distributions were warmer in 1978-1979.

471

472 The LIMS measurements in the winter Arctic region occurred when there was a lot of wave  
473 activity for the transport and mixing of ozone. As a result, ozone varied dramatically in winter,  
474 particularly during times of stratospheric warming events. There was a so-called Canadian  
475 warming in early December 1978, two minor SSW events in late January and early February,  
476 and a final warming in late February 1979. We showed V6 comparisons with temperature and  
477 ozone profile data obtained using rocket borne Datasonde and chemiluminescent instruments,  
478 and we pointed out how an examination of changes in their nearby fields is valuable for the  
479 interpretation and validation of V6 profiles against those correlative measurements. The Level 3  
480 dataset provides daily details on variations of ozone with latitude, longitude, and altitude, along  
481 with related variations in temperature, geopotential height, NO<sub>2</sub>, and HNO<sub>3</sub>. We noted also that  
482 there are instances of spurious, excess ozone from the Level 3 coefficients at 68 hPa in the  
483 tropics but not in the extratropical stratosphere.

484

485 We displayed evidence of a low ozone pocket (LOP) and its chemical properties at 5 hPa above  
486 the Aleutian anticyclone during the minor SSW of late January, and we followed its evolution  
487 into mid-February. The V6 nighttime ozone is relatively accurate through the mesosphere in

488 Arctic winter. We provided time series of the wintertime, tertiary ozone maximum of the upper  
489 mesosphere from V6 data. Its ozone reached maximum values in February, perhaps as a  
490 response to enhanced wave activity in the mesosphere following several SSW events. Together  
491 with V6 maps of T(p) and GPH, one may explore further the daily evolution of that ozone  
492 maximum throughout the NH winter of 1978-1979.

493

#### 494 **Data Availability**

495 The LIMS V6 Level 3 product is at the NASA EARTHDATA site of EOSDIS and its website:  
496 [https://disc.gsfc.nasa.gov/datacollection/LIMSN7L3\\_006.html](https://disc.gsfc.nasa.gov/datacollection/LIMSN7L3_006.html) (Remsberg et al., 2011). The  
497 SPARC-Data Initiative data are located at <https://doi.org/10.5281/zenodo.4265393> (Hegglin et  
498 al., 2021). We acknowledge the individual instrument teams and respective space agencies for  
499 making their measurements available, and the Data Initiative of WCRP's (World Climate  
500 Research Programme) SPARC (Stratospheric Processes and their Role in Climate) project for  
501 organizing and coordinating the compilation of the chemical trace gas datasets used in this work.

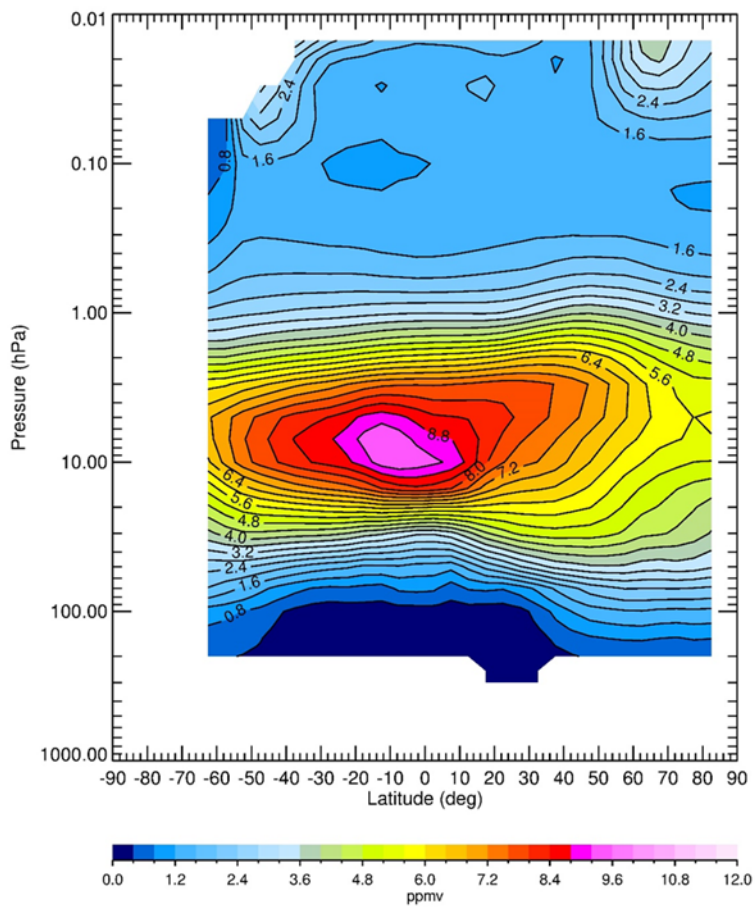
502

503 *Author Contributions.* ER led the manuscript and prepared most of the figures with  
504 contributions from his co-authors. MH conducted the trajectory study and generated its figures.  
505 EH provided his rocketsonde data on ozone and temperature along with their error estimates.

506 *Competing interests.* The authors declare no competing interests for this study.

507 *Acknowledgements.* The authors appreciate John Gille and Jim Russell III and members of the  
508 LIMS Science Team for their leadership in the development of the LIMS instrument and for their  
509 processing of its historic data products. The authors are grateful to John Burton, Praful Bhatt,  
510 Larry Gordley, B. Thomas Marshall, and R. E. Thompson for producing the V6 Level 2 dataset.  
511 They acknowledge Gretchen Lingenfelter for her work in generating and archiving the V6 Level  
512 3 coefficient dataset. They appreciate especially the constructive comments from the two  
513 anonymous referees. They also thank V. Lynn Harvey for her comments on an early draft of the  
514 manuscript. EER and MN carried out their work while serving as Distinguished Research  
515 Associates of the Science Directorate at NASA Langley.

516

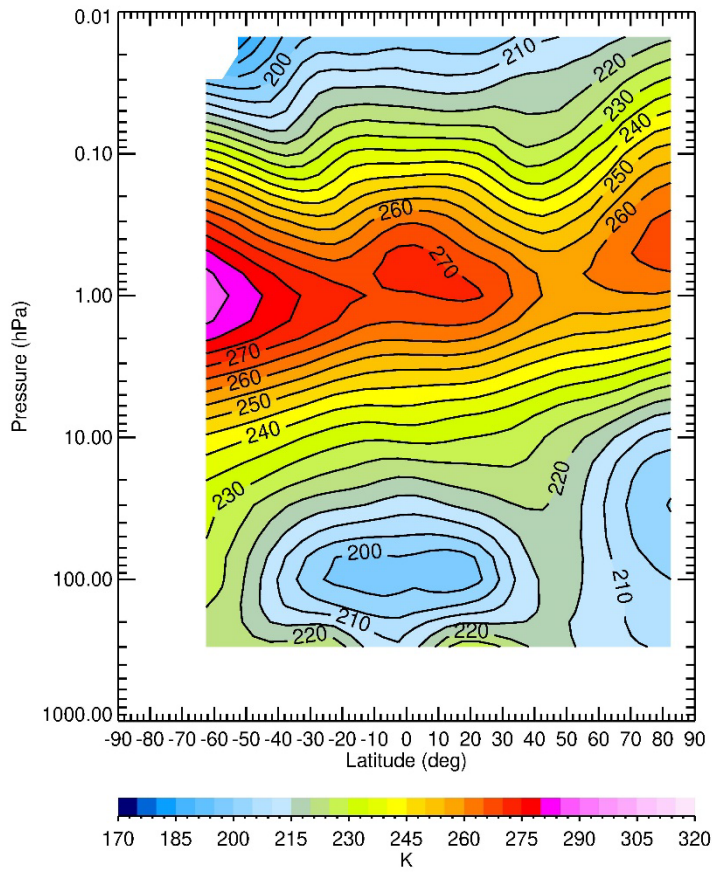


517

518 Figure 1—LIMS V6 Level 3 monthly zonal mean ozone for descending-mode only (or nighttime  
519 equatorward of  $\sim 55^{\circ}\text{S}$ ) for January 1979. Contour interval (CI) is 0.4 ppmv.

520

521

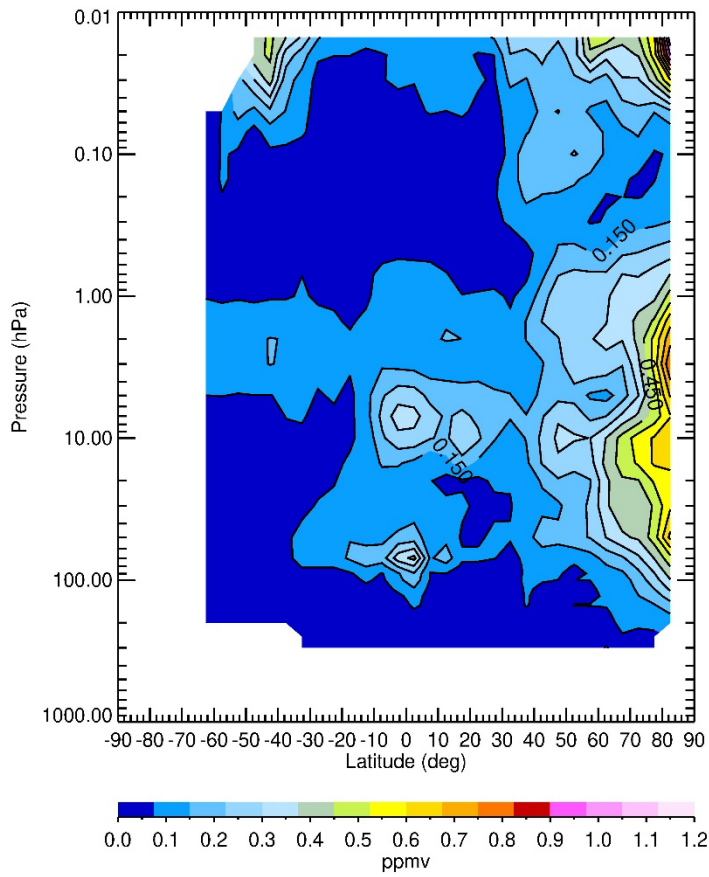


522

523 Figure 2—Zonal average, descending-mode, temperature for January 1979. CI is 5 K.

524

525



526

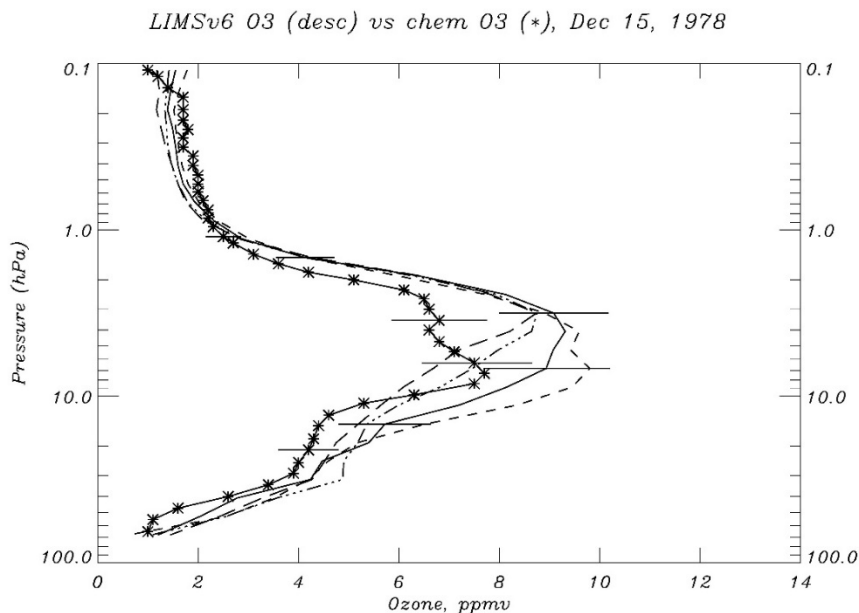
527

528 Figure 3—Zonal standard deviation about average (A+D) zonal mean ozone for January 1979.

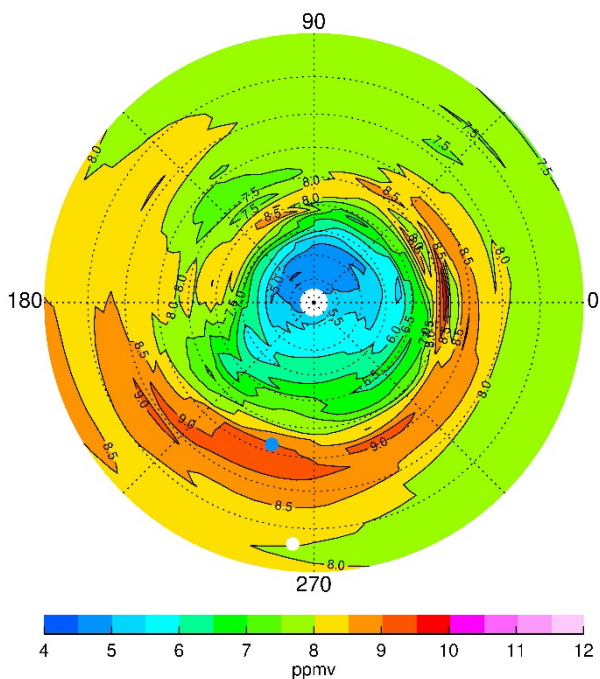
529 CI is 0.075 ppmv.

530

531



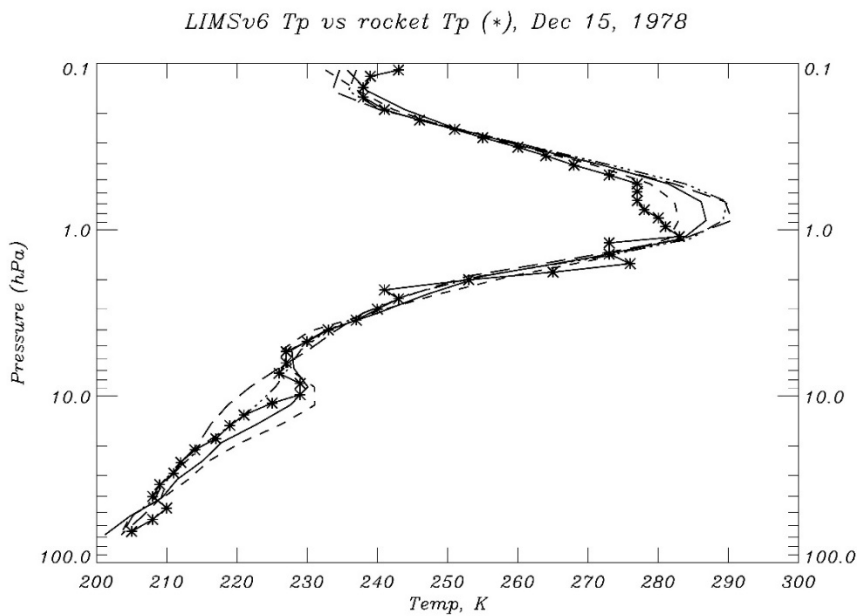
532



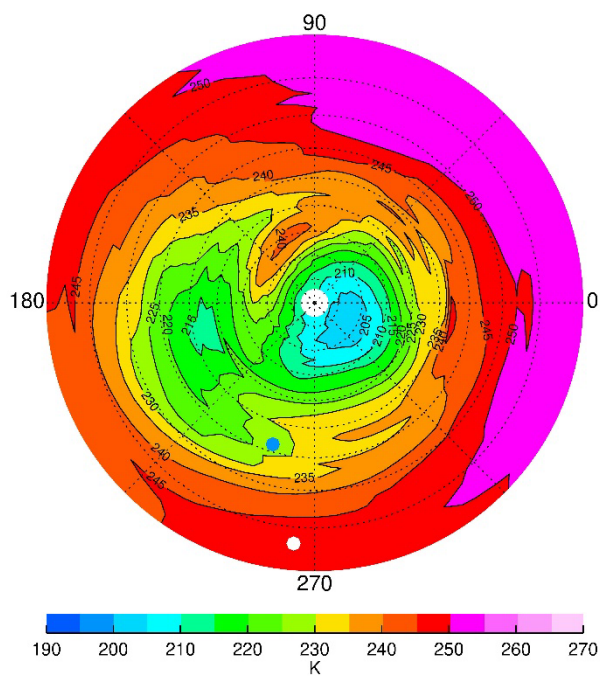
533

534 Figure 4—(top) Profiles of V6 ozone (at 0611Z) versus rocket chem ozone (\* at 0541Z) on  
535 December 15. The four V6 profiles have separations of 2.6° latitude, and the solid curve (at  
536 31.8°N) is closest to White Sands (WS, 32.4°N). Horizontal bars are ozone errors. (bottom) NH  
537 V6 ozone at 4.6 hPa; Greenwich (0°E) is at right, and CI is 0.5 ppmv. Latitude (dotted circles) is  
538 every 10°. Satellite location is white dot (6°N, 265°E), and WS is blue dot.

539



540

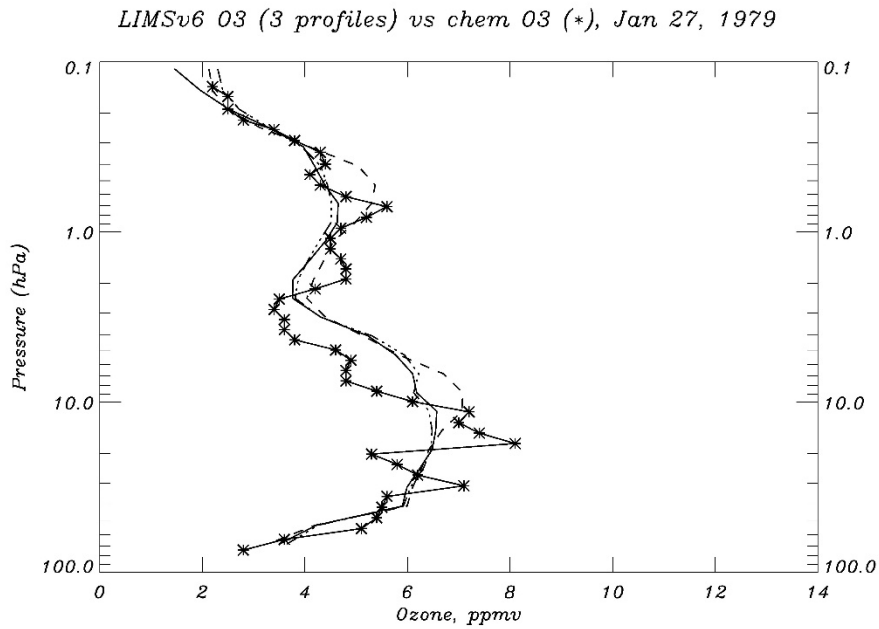


541

542 Figure 5—(top) Profiles of V6 temperature compared with Datasonde values (\*) on December  
543 15. The four V6 profiles are separated as in Fig. 4, where the short-dashed curve is for 29.2° and  
544 the long-dashed curve is for 37.2°. (bottom) NH V6 temperature distribution at 4.6 hPa; CI is 5  
545 K, and satellite location is white dot and White Sands is blue dot.

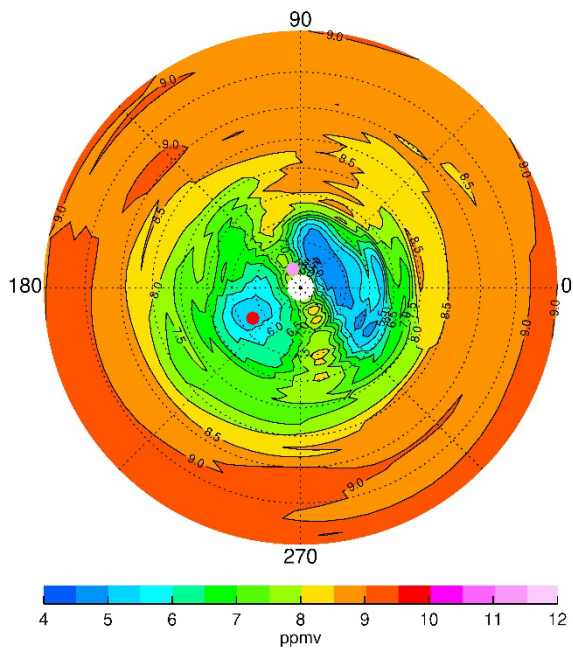


546



547

548



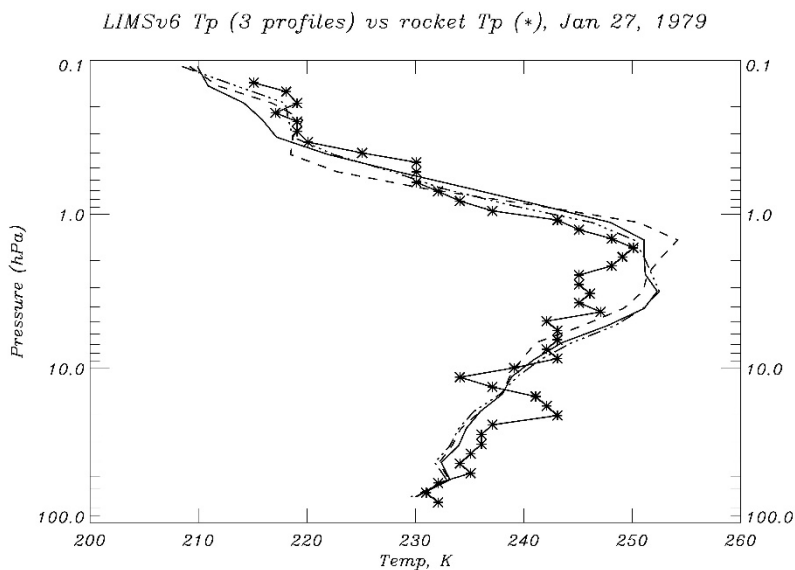
549

550 Figure 6—(top) As in Fig. 4, but for January 27, 1979, at Poker Flat, AK (65°N, 212.5°E);  
551 (bottom) NH V6 distribution of ozone at 4.6 hPa, where CI is 0.5 ppmv. Latitudes (dotted  
552 circles) are spaced every 10°; Poker Flat is red and satellite position (81°N, 113°E) is pink.



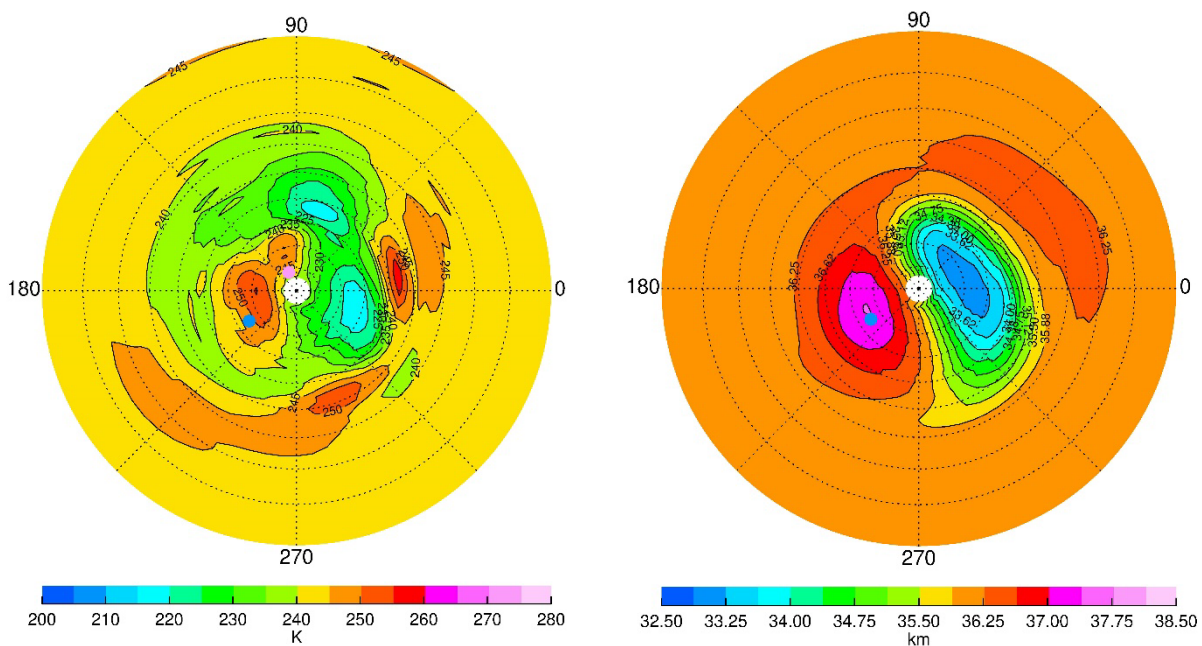
553

554



555

556

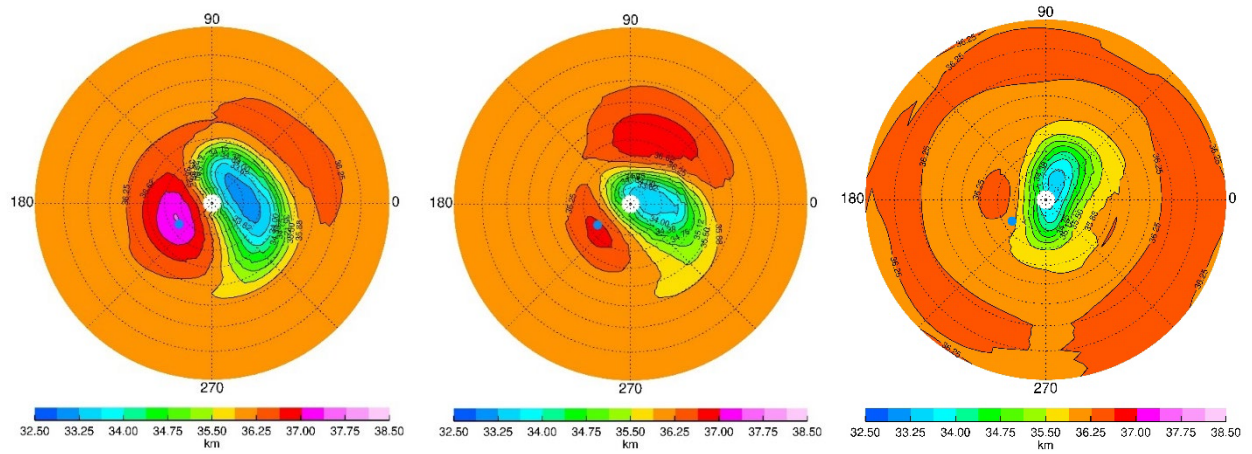


557

558

559 Figure 7—(top) As in Fig. 5, but for January 27, 1979. (bottom-left) NH V6 temperature; CI is 5  
 560 K. Poker Flat is blue and satellite position is pink. (bottom-right) V6 GPH; CI is 0.375 gpkm.

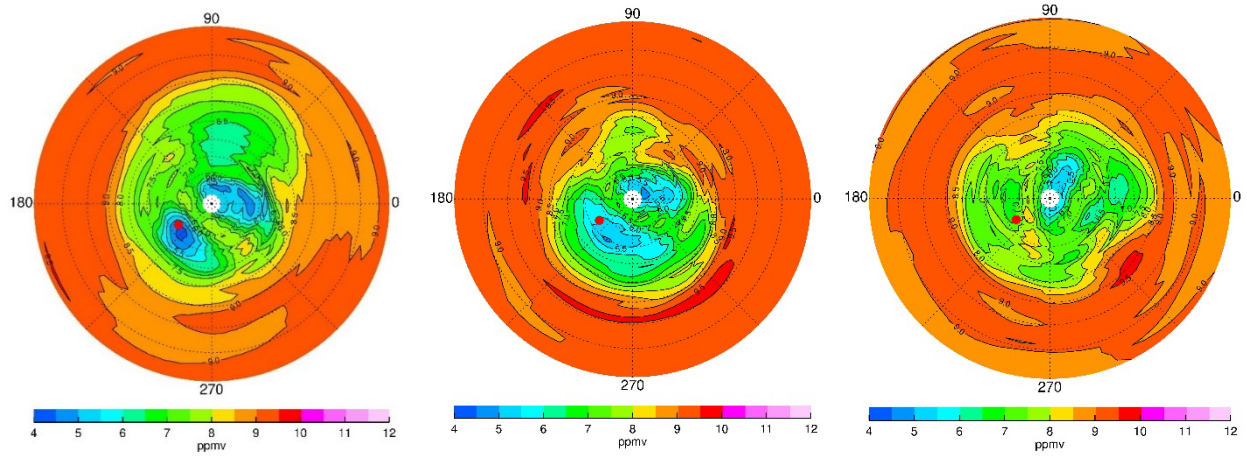
561



562

563 Figure 8—NH V6 GPH at 4.6 hPa; CI is 0.375 gpkm. Poker Flat is blue dot. Panels are spaced  
 564 one week apart; (left) February 3; (middle) February 10; and (right) February 17.

565

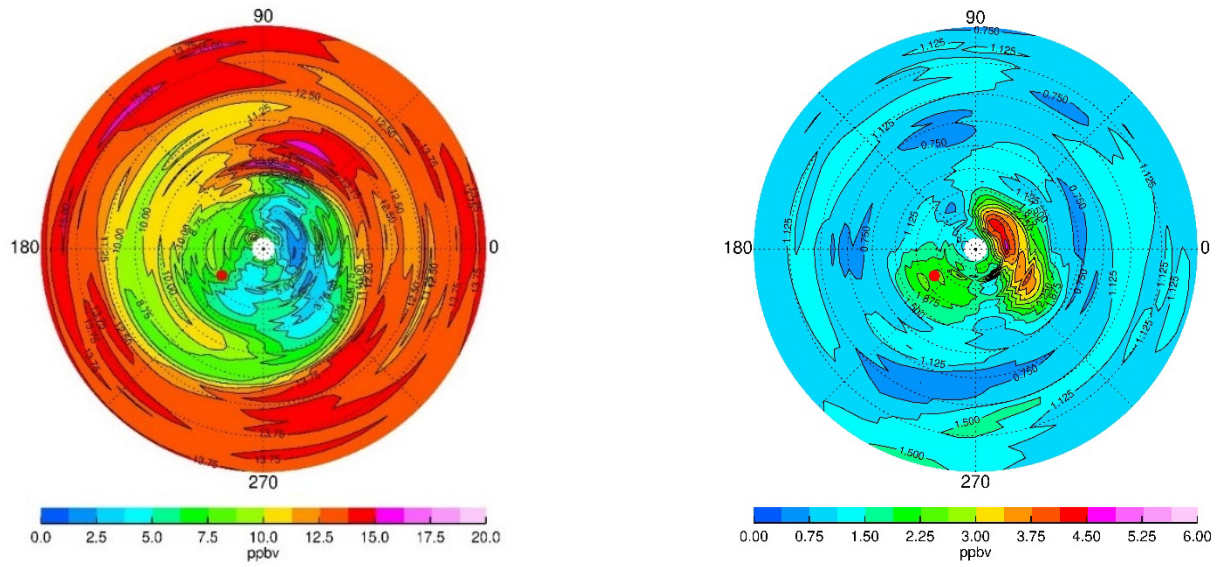


566

567

568 Figure 9—Maps of ozone at 4.6 hPa (left) on February 3, (middle) on February 10; and (right) on  
 569 February 17. CI is 0.5 ppmv and red dot is Poker Flat.

570



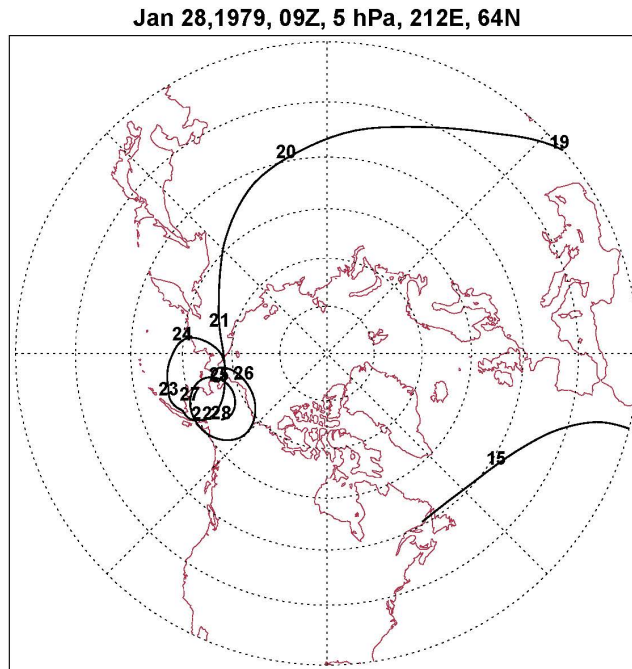
581

582

583 Figure 10—(left) Nighttime NO<sub>2</sub> on January 27 at 4.6 hPa; CI is 1.25 ppbv. (right) HNO<sub>3</sub> at 4.6  
 584 hPa; CI is 0.375 ppbv. Red dot is Poker Flat.

585

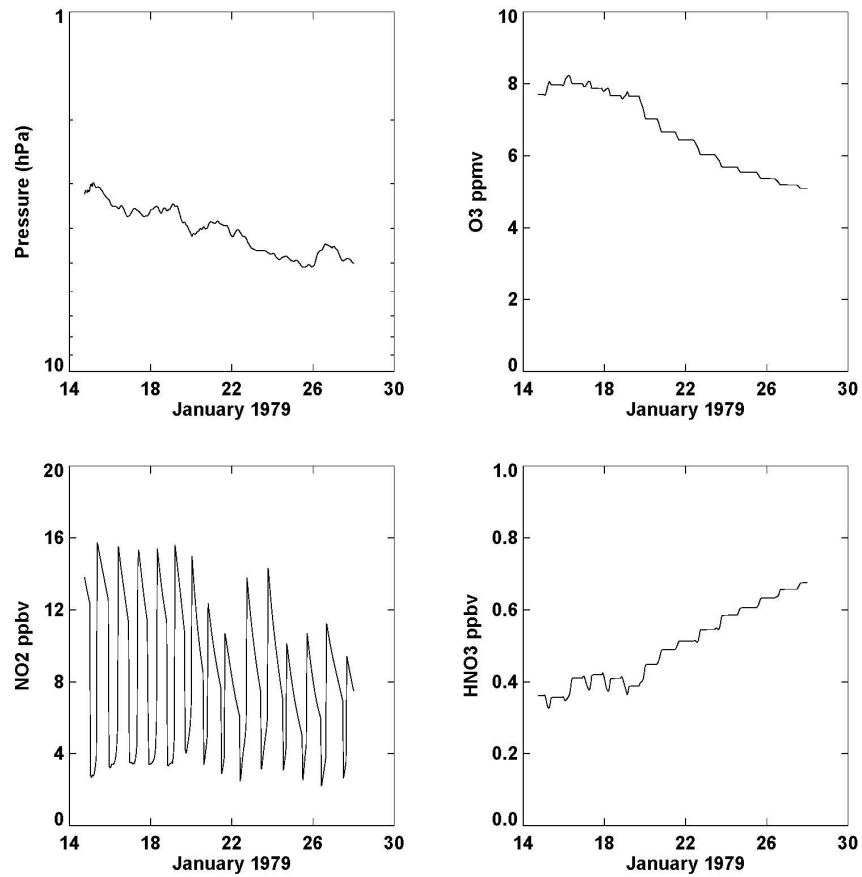
586



588

589 Figure 11—Trajectory of air parcel that end on January 28 at the location of the LOP. Numbers  
590 on the trajectory denote the date, beginning with January 15 and where the parcel is equatorward  
591 of 30°N on January 16-18.

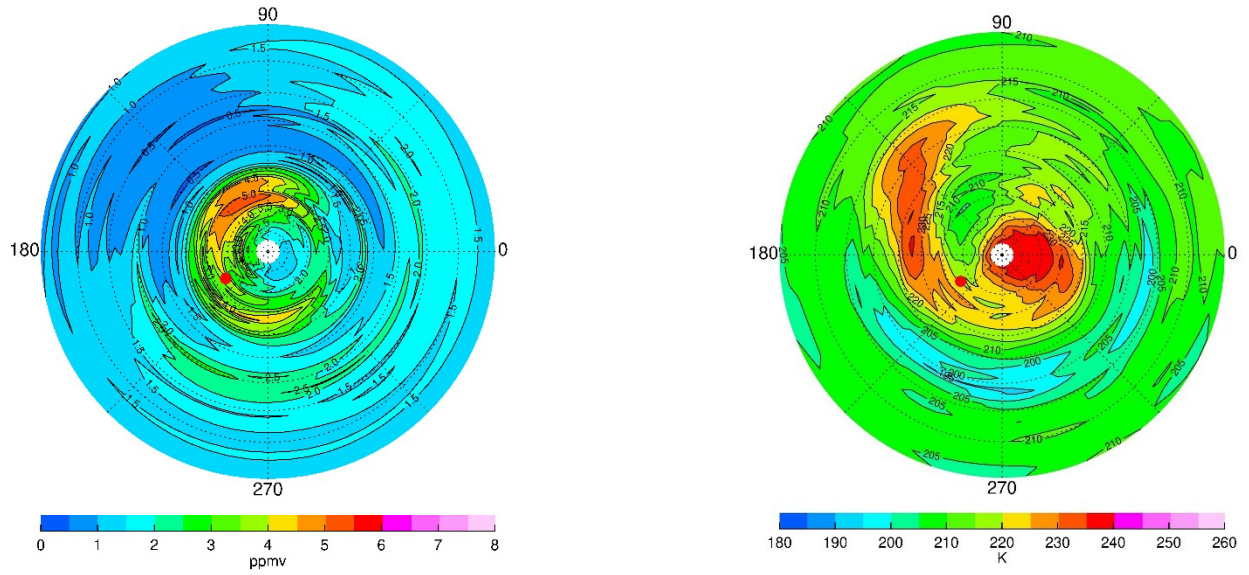
592



594

595 Figure 12—Air parcel history of the changes in its (top left) pressure, (top right) ozone, (bottom  
596 left) NO<sub>2</sub>, and (bottom right) HNO<sub>3</sub>.

597



606

607 Figure 13—(top) NH distributions for December 15 at 0.022 hPa for (left) ozone and for (right)  
 608 temperature; CIs are 0.5 ppmv and 5 K, respectively. Red dot denotes location of Poker Flat.

609

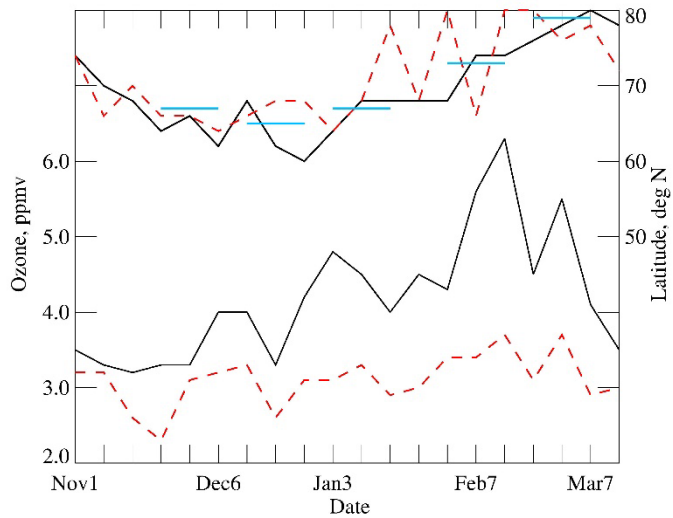
610

611



612

613



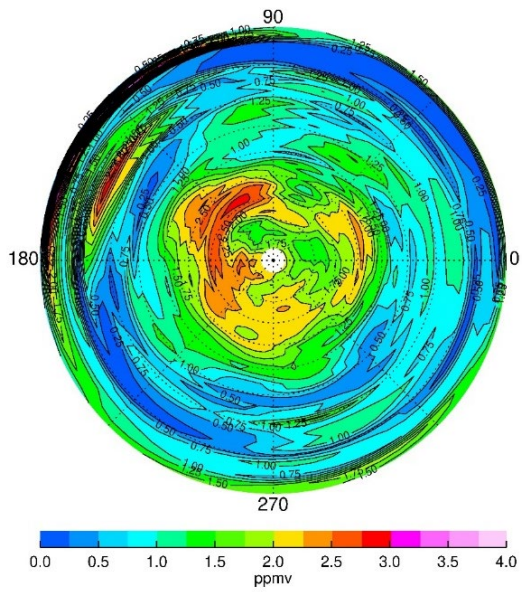
614

615 Figure 14—Time series of peak V6 ozone (bottom two curves) and its latitude location (top two  
616 curves) at 0.022 hPa. Dashed red curves are for combined ozone, while solid curves are for  
617 descending (nighttime) ozone only. Horizontal blue lines indicate the latitude of the terminator.

618



619



620

621

622 Figure 15—NH V6 combined (A+D) ozone distribution at 68 hPa for December 15, 1978. CI is  
623 0.25 ppmv.

624

625 References

626 Andrews, D. G., Holton, J. R., and Leovy, C. B.: *Middle Atmosphere Dynamics*, 1<sup>st</sup> Ed., 489 pp.,  
627 Academic Press, 1987.

628

629 Chandran, A., Collins, R. L., Garcia, R. R., Marsh, D. L., Harvey, V. L., Yue, J., and de la Torre,  
630 L.: A climatology of elevated stratopause events in the whole atmosphere community climate  
631 model, *J. Geophys. Res. Atmos.*, 118, 1234-1246, <https://doi.org/10.1002/jgrd.50123>, 2013.

632

633 de la Cámara, A., Abalos, M., Hitchcock, P., Calvo, N., and Garcia, R. R.: Response of Arctic  
634 ozone to sudden stratospheric warmings, *Atmos. Chem. Phys.*, 18, 16499–16513,  
635 <https://doi.org/10.5194/acp-18-16499-2018>, 2018.

636

637 Edwards, D. P., Kumer, J. B., Lopez-Puertas, M., Mlynchak, M. G., Gopalan, A., Gille, J. C., and  
638 Roche, A.: Non-local thermodynamic equilibrium limb radiance near 10  $\mu\text{m}$  as measured by  
639 UARS CLAES, *J. Geophys. Res.*, 101, D21, 26,577-26,588, <https://doi.org/10.1029/96JD02133>,  
640 1996.

641

642 Fleming, E.L., Chandra, S., Barnett, J. J., and Corney, M.: Zonal mean temperature, pressure,  
643 zonal wind, and geopotential height as functions of latitude, *COSPAR International Reference*  
644 *Atmosphere: 1986, Part II: Middle Atmosphere Models*, *Adv. Space Res.*, 10 (12), 11-59,  
645 [https://doi.org/10.1016/0273-1177\(90\)90386-E](https://doi.org/10.1016/0273-1177(90)90386-E), 1990.

646

647 Funke, B., López-Puertas, M., Garcia-Comas, M., Kaufmann, M., Höpfner, M., and Stiller, G.  
648 P.: GRANADA: a generic RAdiative traNsfer AnD non-LTE population algorithm, *J. Quant.*  
649 *Spectros. Radiat. Transfer*, 113, 1771–1817, <https://doi.org/doi:10.1016/j.jqsrt.2012.05.001>,  
650 2012.

651

652 Gettelman, A., Hoor, P., Pan, L. L., Randel, W. J., Hegglin, M. I., and Birner, T.: The  
653 extratropical upper troposphere and lower stratosphere, *Rev. Geophys.*, 49, RG3033,  
654 <https://doi.org/10.1029/2011RG000355>, 2011.

655

656 Gille, J. C. and Russell III, J. M.: The limb infrared monitor of the stratosphere: experiment  
657 description, performance, and results, *J. Geophys. Res.*, 84, 5125-5140,  
658 <https://doi.org/10.1029/JD089iD04p05125>, 1984.

659

660 Harvey, V. L., Pierce, R. B., Hitchman, M. H., Randall, C. E., and Fairlie, T. D.: On the  
661 distribution of ozone in stratospheric anticyclones, *J. Geophys. Res.*, 109, D24308,  
662 <https://doi.org/10.1029/2004JD004992>, 2004.

663

664 Harvey, V. L., Randall, C. E., Manney, G. L., and Singleton, C. S.: Low-ozone pockets observed  
665 by EOS-MLS, *J. Geophys. Res.*, 113, D17112, <https://doi.org/10.1029/2007JD009181>, 2008.

666

667 Hegglin, M. I., Tegtmeier, S., Anderson, J., Bourassa, A. E., Brohede, S., Degenstein, D.,  
668 Froidevaux, L., Funke, B., Gille, J., Kasai, Y., Kyrola, E. T., Lumpe, J., Murtagh, D., Neu, J. L.,  
669 Perot, K., Remsberg, E. E., Rozanov, A., Toohey, M., Urban, J., von Clarmann, T., Walker, K.  
670 A., Wang, H-J., Arosio, C., Damadeo, R., Fuller, R. A., Lingenfelter, G., McLinden, C.,  
671 Pendelbury, D., Roth, C., Ryan, N. J., Sioris, C., Smith, L., and Weigel, K.: Overview and update  
672 of the SPARC Data Initiative: comparison of stratospheric composition measurements from  
673 satellite limb sounders, *Earth Syst. Sci. Data*, 13, 1855-1903, [https://doi.org/10.5194/essd-1855-](https://doi.org/10.5194/essd-1855-2021)  
674 [2021](https://doi.org/10.5194/essd-1855-2021), 2021.

675

676 Hilsenrath, E.: Rocket observations of the vertical distribution of ozone in the polar night and  
677 during a mid-winter stratospheric warming, *Geophys. Res. Lett.*, 7, 581-584,  
678 <https://doi.org/10.1029/GL007i008p00581>, 1980.

679

680 Hilsenrath, E., and Kirschner, P. T.: Recent assessment of the performance and accuracy of a  
681 chemiluminescent rocket sonde for upper atmospheric ozone measurements, *Rev. Sci. Instrum.*,  
682 Vol. 51, 1381-1389, <https://doi.org/10.1063/1.1136080>, 1980.

683

684 Hitchman, M. H., Gille, J. C., Rodgers, C. D., and Brasseur, G.: The separated polar winter  
685 stratopause: a wave driven climatological feature, *J. Atmos. Sci.*, 46, 410-422,  
686 [https://doi.org/10.1175/1520-0469\(1989\)046%3C0410:TSPWSA%3E2.0.CO;2](https://doi.org/10.1175/1520-0469(1989)046%3C0410:TSPWSA%3E2.0.CO;2), 1989.

687

688 Holt, L. A., Randall, C. E., Harvey, V. L., Remsberg, E. E., Stiller, G. P., Funke, B., Bernath, P.  
689 F., and Walker, K. A., Atmospheric effects of energetic particle precipitation in the Arctic winter  
690 1978–1979 revisited, *J. Geophys. Res.*, 117, D05315, <https://doi.org/10.1029/2011JD016663>,  
691 2012.

692

693 Kim, J-H., Jee, G., Choi, H., Kim, B-M., and Kim, S-J.: Vertical structures of temperature and  
694 ozone changes in the stratosphere and mesosphere during stratospheric sudden warmings, *J.*  
695 *Astron. Space Sci.*, 37, 69-75, <https://doi.org/10.5140/JASS.2020.37.1.69>, 2020.

696

697 Leovy, C. B., Sun, C-R., Hitchman, M. H., Remsberg, E. E., Russell, III, J. M., Gordley, L. L.,  
698 Gille, J. C., and Lyjak, L. V.: Transport of ozone in the middle stratosphere: evidence for  
699 planetary wave breaking, *J. Atmos. Sci.*, 42, 230-244, [https://doi.org/10.1175/1520-0469\(1985\)042%3C0230:TOOITM%3E2.0.CO;2](https://doi.org/10.1175/1520-0469(1985)042%3C0230:TOOITM%3E2.0.CO;2), 1985.

701

702 Lieberman, R. S., Oberheide, J., Hagan, M. E., Remsberg, E. E., and Gordley, L. L.: Variability  
703 of diurnal tides and planetary waves during November 1978–May 1979, *J. Atmos. Solar-Terr.*  
704 *Phys.*, 66, 517–528, <https://doi.org/10.1016/j.jastp.2004.01.006>, 2004.

705

706 Lopez-Puertas, M. and Taylor, F. W.: Non-LTE Radiative transfer in the Atmosphere, World  
707 Scientific Publ. Co., River Edge, NJ, USA, 504 pp., 2001.

708

709 López-Puertas, M., García-Comas, M., Funke, B., Gardini, A., Stiller, G. P., Clarmann, T. von,  
710 Glatthor, N., Laeng, A., Kaufmann, M., Sofieva, V. F., Froidevaux, L., Walker, K. A., and  
711 Shiotani, M.: MIPAS observations of ozone in the middle atmosphere, *Atmos. Meas. Tech.*, 11,  
712 2187–2212, <https://doi.org/10.5194/amt-11-2187-2018>, 2018.

713

714 Manney, G. L., Froidevaux, L., Waters, J. W., Zurek, R. W., Gille, J. C., Kumer, J. B.,  
715 Mergenthaler, J. L., Roche, A. E., O'Neill, A., and Swinbank, R.: Formation of low-ozone  
716 pockets in the middle stratospheric anticyclone during winter, *J. Geophys. Res. Atmos.*, 100,  
717 13939-13950, <https://doi.org/10.1029/95JD00372>, 1995.

718

719 Marsh, D., Smith, A., Brasseur, G., Kaufmann, M., and Grossmann, K.: The existence of a  
720 tertiary ozone maximum in the high-latitude middle mesosphere, *Geophys. Res. Lett.*, 28, 4531-  
721 4534, <https://doi.org/10.1029/2001GL013791>, 2001.

722

723 Manuilova, R. O., Gusev, O. A., Kutepov, A. A., von Clarmann, T., Oelhaf, H., Stiller, G. P.,  
724 Wegner, A., Lopez-Puertas, M., Martin-Torres, F. J., Zaragoza, G., and Flaud, J.-M.: Modelling  
725 of non-LTE limb spectra of i.r. ozone bands for the MIPAS space experiment, *J. Quant.*  
726 *Spectrosc. Rad. Transf.*, 59, 405-422, [https://doi.org/10.1016/S0022-4073\(97\)00120-9](https://doi.org/10.1016/S0022-4073(97)00120-9), 1998.

727

728 Mlynczak, M. G. and Drayson, R.: Calculation of infrared limb emission by ozone in the  
729 terrestrial middle atmosphere 2. Emission calculations, *J. Geophys. Res.*, 95, 16,513-16,521,  
730 <https://doi.org/10.1029/JD095iD10p16513>, 1990.

731

732 Morris, G. A., Kawa, S. R., Douglass, A. R., Schoeberl, M. R., Froidevaux, L., and Waters, J.,  
733 Low-ozone pockets explained, *J. Geophys. Res.*, 103, 3599-3610,  
734 <https://doi.org/10.1029/97JD02513>, 1998.

735

736 Nair, H., Allen, M., Froidevaux, L., and Zurek, R.: Localized rapid ozone loss in the northern  
737 winter stratosphere: An analysis of UARS observations, *J. Geophys. Res.*, 103, 1555-1571,  
738 <https://doi.org/10.1029/97JD03072>, 1998.

739

740 Remsberg, E., and Lingenfelter, G.: LIMS Version 6 Level 3 dataset, NASA-TM-2010-216690,  
741 available at <http://www.sti.nasa.gov> (last access: 17 September 2019), 13 pp., 2010.

742

743 Remsberg, E. E., Haggard, K. V., and Russell III, J. M.: Estimation of synoptic fields of middle  
744 atmosphere parameters from Nimbus-7 LIMS profile data, *J. Atmos. Ocean. Tech.*, 7, 689-705,  
745 [https://doi.org/10.1175/1520-0426\(1990\)007%3C0689:EOSFOM%3E2.0.CO;2](https://doi.org/10.1175/1520-0426(1990)007%3C0689:EOSFOM%3E2.0.CO;2), 1990.

746

747 Remsberg, E. E., Gordley, L. L., Marshall, B. T., Thompson, R. E., Burton, J., Bhatt, P., Harvey,  
748 V. L., Lingenfelter, G., Natarajan, M.: The Nimbus 7 LIMS version 6 radiance conditioning and  
749 temperature retrieval methods and results, *J. Quant. Spectros. Rad. Transf.*, 86, 395-424,  
750 doi:10.1016/j.jqsrt.2003.12.007, 2004.

751

752 Remsberg, E., Lingenfelter, G., Natarajan, M., Gordley, L., Marshall, B. T., and Thompson, E.:  
753 On the quality of the Nimbus 7 LIMS version 6 ozone for studies of the middle atmosphere, *J.*  
754 *Quant. Spectros. Rad. Transf.*, 105, 492-518, doi:10.1016/j.jqsrt.2006.12.005, 2007.

755

756 Remsberg, E., Lingenfelter, G., and Natarajan, M.: LIMS/Nimbus-7 Level 3 Daily 2 deg  
757 Latitude Zonal Fourier Coefficients of O3, NO2, H2O, HNO3, Geopotential Height, and  
758 Temperature V006, Version: 006, Goddard Earth Sciences Data and Information Services Center

759 (GES DISC), available at: [https://disc.gsfc.nasa.gov/datacollection/LIMSN7L3\\_006.html](https://disc.gsfc.nasa.gov/datacollection/LIMSN7L3_006.html) (last  
760 access: 11 March 2021), 2011.

761

762 Remsberg, E., Natarajan, M., Fairlie, T. D., Wargan, K., Pawson, S., Coy, L., Lingenfelter, G.,  
763 and Kim, G.: On the inclusion of Limb Infrared Monitor of the Stratosphere version 6 ozone in a  
764 data assimilation system, *J. Geophys. Res.*, 118, 7982-8000, <https://doi.org/10.1002/jgrd.50566>,  
765 2013.

766

767 Remsberg, E., Natarajan, M., and Harvey, V. L.: On the consistency of HNO<sub>3</sub> and NO<sub>2</sub> in the  
768 Aleutian High region from the Nimbus 7 LIMS Version 6 dataset, *Atmos. Meas. Tech.*, 11,  
769 3611-3626, <https://doi.org/10.5194/amt-11-3611-2018>, 2018.

770

771 Remsberg, E., Harvey, V. L., Krueger, A., and Natarajan, M.: Residual temperature bias effects  
772 in stratospheric species distributions from LIMS, *Atmos. Meas. Tech.*, 14, 2185-2199,  
773 <https://doi.org/10.5194/amt-14-2185-2021>, 2021.

774

775 Shams, S. B., von Walden, P., Hannigan, J. W., Randel, W. J., Petropavlovskikh, I. V., Butler, A.  
776 H., and de la Cámara, A.: Analyzing ozone variations and uncertainties at high latitudes during  
777 sudden stratospheric warming events using MERRA-2, *Atmos. Chem. Phys. Disc.*,  
778 <https://doi.org/10.5194/acp-2021-646>, 2021.

779

780 Shepherd, T. G., Plummer, D. A., Scinocca, J. F., Hegglin, M. I., Fioletov, V. E., Reader, M. C.,  
781 Remsberg, E., von Clarmann, T., and Wang, H. J.: Reconciliation of halogen-induced ozone loss  
782 with the total-column record, *Nature Geoscience*, 7, 443-449, doi:10.1038/ngeo2155, 2014.

783

784 Siskind, D. E., Coy, L., Espy, P.: Observations of stratospheric warmings and mesospheric  
785 coolings by the TIMED SABER instrument, *Geophys. Res. Lett.* 32,  
786 <http://doi.org/10.1029/2005GL022399>, 2005.

787

788 Siskind, D. E., Harvey, V. L., Sassi, F., McCormack, J. P., Randall, C. E., Hervig, M. E., and  
789 Bailey, S. M.: Two- and three-dimensional structures of the descent of mesospheric trace  
790 constituents after the 2013 sudden stratospheric warming elevated stratopause event, *Atmos.*  
791 *Chem. Phys.*, 21, 14059–14077, <https://doi.org/10.5194/acp-21-14059-2021>, 2021.

792

793 Smith, A. K., López-Puertas, M., García-Comas, M., and Tukiainen, S.: SABER observations of  
794 mesospheric ozone during NH late winter 2002–2009, *Geophys. Res. Lett.*, 36, L23804,  
795 <https://doi.org/10.1029/2009GL040942>, 2009.

796

797 Smith, A. K., Garcia, R. R., Marsh, D. R., and Richter, J. A.: WACCM simulations of the mean  
798 circulation and trace species transport in the winter mesosphere, *J. Geophys. Res.*, 116, D20115,  
799 <https://doi.org/10.1029/2011JD016083>, 2011.

800

801 Smith, A. K., Espy, P. J., López-Puertas, M., and Tweedy, O. V., Spatial and temporal structure  
802 of the tertiary ozone maximum in the polar winter mesosphere, *J. Geophys. Res.*, 123, 4373-  
803 4389, <https://doi.org/10.1029/2017JD028030>, 2018.

804

805 Sofieva, V. F., Szela, M., Tamminen, J., Kyrölä, E., Degenstein, D., Roth, C., Zawada, D.,  
806 Rozanov, A., Arosio, C., Burrows, J. P., Weber, M., Laeng, A., Stiller, G. P., von Clarmann, T.,  
807 Froidevaux, L., Livesey, N., van Roozendaal, M., and Retscher, C.: Measurement report:  
808 regional trends of stratospheric ozone evaluated using the MErged GRIdded Dataset of Ozone  
809 Profiles (MEGRIDOP), *Atmos. Chem. Phys.*, 21, 6707–6720, [https://doi.org/10.5194/acp-21-](https://doi.org/10.5194/acp-21-6707-2021)  
810 [6707-2021](https://doi.org/10.5194/acp-21-6707-2021), 2021.



811

812 Solomon, S., Kiehl, J. T., Kerridge, B. J., Remsberg, E. E., and Russell III, J. M.: Evidence for  
813 nonlocal thermodynamic equilibrium in the  $\nu_3$  mode of mesospheric ozone, *J. Geophys. Res.*, 91,  
814 9865-9876, <https://doi.org/10.1029/JD091iD09p09865>, 1986.

815

816 SPARC, Assessment of Stratospheric Aerosol Properties, L. Thomason and Th. Peter, Ed.,  
817 WCRP-124, WMO/TD- No. 1295, SPARC Report No. 4, 322 pp., 2006.

818

819 SPARC: The SPARC Data Initiative: Assessment of stratospheric trace gas and aerosol  
820 climatologies from satellite limb sounders, Hegglin, M. I. and Tegtmeier, S., (Eds.), SPARC  
821 Report No. 8, WCRP-5/2017, <http://www.sparc-climate.org/publications/sparc-reports/>, 2017.

822

823 Stolarski, R. S., Douglass, A. R., Remsberg, E. E., Livesey, N. J., and Gille, J. C.: Ozone  
824 temperature correlations in the upper stratosphere as a measure of chlorine content, *J. Geophys.*  
825 *Res.*, 117, D10305, <https://doi.org/10.1029/2012JD017456>. 2012.

826

827 Tegtmeier, S., Hegglin, M. I., Anderson, J., Bourassa, A., Brohede, S., Degenstein, D.,  
828 Froidevaux, L., Fuller, R., Funke, B., Gille, J., Jones, A., Kasai, Y., Krüger, K., Kyrölä, E.,  
829 Lingenfelter, G., Lumpe, J., Nardi, B., Neu, J., Pendlebury, D., Remsberg, E., Rozanov, A.,  
830 Smith, L., Toohey, M., Urban, J., von Clarmann, T., Walker, K. A. and Wang, R. H. H.: SPARC  
831 Data Initiative: A comparison of ozone climatologies from international satellite limb sounders,  
832 *J. Geophys. Res.*, 118, 12,229-12,247, <https://doi.org/10.1002/2013JD019877>, 2013.

833

834 WOUDC, World Ozone and Ultraviolet Radiation Data Centre, <https://woudc.org/home.php>.

835